

Multiple-scattering suppressive refractive index tomography for the label-free quantitative assessment of multicellular spheroids: supplement

OSAMU YASUHIKO,*  KOZO TAKEUCHI, HIDENAO YAMADA, AND YUKIO UEDA

Central Research Laboratory, Hamamatsu Photonics K.K., 5000 Hirakuchi, Hamakita-ku, Hamamatsu, Shizuoka 434-8601, Japan

**osamu.yasuhiko@crl.hpk.co.jp*

This supplement published with Optica Publishing Group on 25 January 2022 by The Authors under the terms of the [Creative Commons Attribution 4.0 License](#) in the format provided by the authors and unedited. Further distribution of this work must maintain attribution to the author(s) and the published article's title, journal citation, and DOI.

Supplement DOI: <https://doi.org/10.6084/m9.figshare.18626729>

Parent Article DOI: <https://doi.org/10.1364/BOE.446622>

Multiple-scattering suppressive refractive index tomography for label-free quantitative assessment of multicellular spheroids: supplemental document

1. Conventional formulation of Rytov approximation

The conventional formulation of ODT using Rytov approximation is described here. We first derive the Born approximation and then the conventional Rytov approximation using perturbation theory. The formula provided here is based on a previous study [1]. We introduce a dimensionless parameter λ and expand $u(\mathbf{r}; \mathbf{k}_{\text{in}}^j)$ as the power series in λ :

$$\begin{aligned} u(\mathbf{r}; \mathbf{k}_{\text{in}}^j) &= u_0(\mathbf{r}; \mathbf{k}_{\text{in}}^j) + \lambda u_1(\mathbf{r}; \mathbf{k}_{\text{in}}^j) + \lambda^2 u_2(\mathbf{r}; \mathbf{k}_{\text{in}}^j) + \dots \\ &= \sum_l \lambda^l u_l(\mathbf{r}; \mathbf{k}_{\text{in}}^j). \end{aligned} \quad (\text{S1})$$

We treat the scattering potential $V(\mathbf{r})$ as a perturbation: $V(\mathbf{r}) \rightarrow \lambda V(\mathbf{r})$. In this case, on substituting Eq. (S1) in Eq. (1), we obtain

$$\sum_l \lambda^l u_l(\mathbf{r}; \mathbf{k}_{\text{in}}^j) = u_{\text{in}}(\mathbf{r}; \mathbf{k}_{\text{in}}^j) + \int d\mathbf{r}' G(\mathbf{r} - \mathbf{r}') \lambda V(\mathbf{r}') \sum_l \lambda^l u_l(\mathbf{r}'; \mathbf{k}_{\text{in}}^j). \quad (\text{S2})$$

We can solve Eq.

(S2) by comparing the coefficients of each power of λ .

Order λ^0 : At order λ^0 , we have

$$u_0(\mathbf{r}; \mathbf{k}_{\text{in}}^j) = u_{\text{in}}(\mathbf{r}; \mathbf{k}_{\text{in}}^j). \quad (\text{S3})$$

Order λ^1 : At order λ^1 , we have

$$\begin{aligned} u_1(\mathbf{r}; \mathbf{k}_{\text{in}}^j) &= \int d\mathbf{r}' G(\mathbf{r} - \mathbf{r}') V(\mathbf{r}') u_0(\mathbf{r}'; \mathbf{k}_{\text{in}}^j) \\ &= \int d\mathbf{r}' G(\mathbf{r} - \mathbf{r}') V(\mathbf{r}') u_{\text{in}}(\mathbf{r}'; \mathbf{k}_{\text{in}}^j). \end{aligned} \quad (\text{S4})$$

The Born approximation of Eq. (1) is given by the first-order approximation of Eq. (S1). We set $\lambda \rightarrow 1$ and obtain

$$\begin{aligned} u(\mathbf{r}; \mathbf{k}_{\text{in}}^j) &\cong u_{\text{Born}}(\mathbf{r}; \mathbf{k}_{\text{in}}^j) \\ &:= u_0(\mathbf{r}; \mathbf{k}_{\text{in}}^j) + u_1(\mathbf{r}; \mathbf{k}_{\text{in}}^j) \\ &= u_{\text{in}}(\mathbf{r}; \mathbf{k}_{\text{in}}^j) + \int d\mathbf{r}' G(\mathbf{r} - \mathbf{r}') V(\mathbf{r}') u_{\text{in}}(\mathbf{r}'; \mathbf{k}_{\text{in}}^j). \end{aligned} \quad (\text{S5})$$

Next, we derive the Rytov approximation of Eq. (1). We expand $u(\mathbf{r}; \mathbf{k}_{\text{in}}^j)$ as a power series in λ , as follows:

$$\begin{aligned} u(\mathbf{r}; \mathbf{k}_{\text{in}}^j) &= \exp(\phi_0(\mathbf{r}; \mathbf{k}_{\text{in}}^j) + \lambda \phi_1(\mathbf{r}; \mathbf{k}_{\text{in}}^j) + \lambda^2 \phi_2(\mathbf{r}; \mathbf{k}_{\text{in}}^j) + \dots) \\ &= \exp\left(\sum_l \lambda^l \phi_l(\mathbf{r}; \mathbf{k}_{\text{in}}^j)\right). \end{aligned} \quad (\text{S6})$$

We then equate Eq.

(S2) and (S6), solve it by comparing coefficients of each power of λ .

Order λ^0 : At order λ^0 , we have

$$\phi_0(\mathbf{r}; \mathbf{k}_{\text{in}}^j) = \ln(u_0(\mathbf{r}; \mathbf{k}_{\text{in}}^j)). \quad (\text{S7})$$

Order λ^1 : At order λ^1 , we have

$$\phi_1(\mathbf{r}; \mathbf{k}_{\text{in}}^j) = \frac{u_1(\mathbf{r}; \mathbf{k}_{\text{in}}^j)}{u_0(\mathbf{r}; \mathbf{k}_{\text{in}}^j)}. \quad (\text{S8})$$

The Rytov approximation of Eq. (1) is given by the first-order approximation of Eq. (S6). We set $\lambda \rightarrow 1$ and obtain

$$\begin{aligned} u(\mathbf{r}; \mathbf{k}_{\text{in}}^j) &\cong u_{\text{Rytov}}(\mathbf{r}; \mathbf{k}_{\text{in}}^j) \\ &:= \exp(\phi_0(\mathbf{r}; \mathbf{k}_{\text{in}}^j) + \phi_1(\mathbf{r}; \mathbf{k}_{\text{in}}^j)) \\ &= u_{\text{in}}(\mathbf{r}; \mathbf{k}_{\text{in}}^j) \exp\left(\frac{1}{u_{\text{in}}(\mathbf{r}; \mathbf{k}_{\text{in}}^j)} \int d\mathbf{r}' G(\mathbf{r} - \mathbf{r}') V(\mathbf{r}') u_{\text{in}}(\mathbf{r}'; \mathbf{k}_{\text{in}}^j)\right). \end{aligned} \quad (\text{S9})$$

In this conventional formulation, the Rytov approximation is applied to coherent fields $u(\mathbf{r}; \mathbf{k}_{\text{in}}^j)$. The validity of Rytov approximation depends on the smoothness of the fields. Further, as field $u(\mathbf{r}; \mathbf{k}_{\text{in}}^j)$ is vulnerable to MS owing to its high coherence, this conventional formulation becomes invalid when the sample shows MS.

2. Formulation of cMSS-Rytov

Here, we formulate cMSS-Rytov, such that the theory of ODT is compatible with the coherent MSS technique used as in CASS. We expand $\bar{u}(\mathbf{r}; \mathbf{k}_{\text{in}}^j)$ as a power series in λ :

$$\begin{aligned} \bar{u}(\mathbf{r}; \mathbf{k}_{\text{in}}^j) &= \bar{u}_0(\mathbf{r}; \mathbf{k}_{\text{in}}^j) + \lambda \bar{u}_1(\mathbf{r}; \mathbf{k}_{\text{in}}^j) + \lambda^2 \bar{u}_2(\mathbf{r}; \mathbf{k}_{\text{in}}^j) + \dots \\ &= \sum_l \lambda^l \bar{u}_l(\mathbf{r}; \mathbf{k}_{\text{in}}^j). \end{aligned} \quad (\text{S10})$$

From Eq. (S3) and (S4), using the relationships $\bar{u}(\mathbf{r}; \mathbf{k}_{\text{in}}^j) := u(\mathbf{r}; \mathbf{k}_{\text{in}}^j) \exp(-i\mathbf{k}_{\text{in}}^j \cdot \mathbf{r})$ and $u_{\text{in}}(\mathbf{r}; \mathbf{k}_{\text{in}}^j) := a_0 \exp(i\mathbf{k}_{\text{in}}^j \cdot \mathbf{r})$, we obtain the following equations:

$$\bar{u}_0(\mathbf{r}; \mathbf{k}_{\text{in}}^j) = u_0(\mathbf{r}; \mathbf{k}_{\text{in}}^j) \exp(-i\mathbf{k}_{\text{in}}^j \cdot \mathbf{r}) = a_0, \quad (\text{S11})$$

$$\bar{u}_1(\mathbf{r}; \mathbf{k}_{\text{in}}^j) = a_0 \int d\mathbf{r}' \bar{G}(\mathbf{r} - \mathbf{r}'; \mathbf{k}_{\text{in}}^j) V(\mathbf{r}'). \quad (\text{S12})$$

We expand $\bar{U}^{\text{cMSS}}(\mathbf{r})$ as a power series in λ :

$$\begin{aligned} \bar{U}^{\text{cMSS}}(\mathbf{r}) &= \bar{U}_0^{\text{cMSS}}(\mathbf{r}) + \lambda \bar{U}_1^{\text{cMSS}}(\mathbf{r}) + \lambda^2 \bar{U}_2^{\text{cMSS}}(\mathbf{r}) + \dots \\ &= \sum_l \lambda^l \bar{U}_l^{\text{cMSS}}(\mathbf{r}). \end{aligned} \quad (\text{S13})$$

Substituting Eq. (S13) and (S10) in Eq. (2), we obtain

$$\sum_l \lambda^l \bar{U}_l^{\text{cMSS}}(\mathbf{r}) = \frac{1}{N_{\text{in}}} \sum_j \sum_l \lambda^l \bar{u}_l(\mathbf{r}; \mathbf{k}_{\text{in}}^j). \quad (\text{S14})$$

We can now solve Eq.

(S14) by comparing coefficients of each power of λ .

Order λ^0 : At order λ^0 , we have

$$\bar{U}_0^{\text{cMSS}}(\mathbf{r}) = \frac{1}{N_{\text{in}}} \sum_j \bar{u}_0(\mathbf{r}; \mathbf{k}_{\text{in}}^j) = a_0, \quad (\text{S15})$$

obtained using Eq. (S11).

Order λ^1 : At order λ^1 , we have

$$\begin{aligned} \bar{U}_1^{\text{cMSS}}(\mathbf{r}) &= \frac{1}{N_{\text{in}}} \sum_j \bar{u}_1(\mathbf{r}; \mathbf{k}_{\text{in}}^j) \\ &= a_0 \int d\mathbf{r}' V(\mathbf{r}') \frac{1}{N_{\text{in}}} \sum_j \bar{G}(\mathbf{r} - \mathbf{r}'; \mathbf{k}_{\text{in}}^j), \end{aligned} \quad (\text{S16})$$

obtained using Eq. (S12).

The Born approximation of Eq. (2) is given by the first-order approximation of Eq.(S13). We set $\lambda \rightarrow 1$ and obtain $\bar{U}_{\text{Born}}^{\text{cMSS}}(\mathbf{r})$:

$$\begin{aligned} \bar{U}_{\text{Born}}^{\text{cMSS}}(\mathbf{r}) &:= \bar{U}_0^{\text{cMSS}}(\mathbf{r}) + \bar{U}_1^{\text{cMSS}}(\mathbf{r}) \\ &= a_0 + a_0 \int d\mathbf{r}' V(\mathbf{r}') \frac{1}{N_{\text{in}}} \sum_j \bar{G}(\mathbf{r} - \mathbf{r}'; \mathbf{k}_{\text{in}}^j). \end{aligned} \quad (\text{S17})$$

Next, we derive the Rytov approximation of Eq. (2). We expand $\bar{U}^{\text{cMSS}}(\mathbf{r})$ as a power series in λ , as follows:

$$\begin{aligned} \bar{U}^{\text{cMSS}}(\mathbf{r}) &= \exp(\Phi_0(\mathbf{r}) + \lambda \Phi_1(\mathbf{r}) + \lambda^2 \Phi_2(\mathbf{r}) + \dots) \\ &= \exp\left(\sum_l \lambda^l \Phi_l(\mathbf{r})\right). \end{aligned} \quad (\text{S18})$$

We then equate Eq. (S13) and (S18) and solve it by comparing coefficients of each power of λ .

Order λ^0 : At order λ^0 , we have

$$\Phi_0(\mathbf{r}) = \ln(\bar{U}_0^{\text{cMSS}}(\mathbf{r})). \quad (\text{S19})$$

Order λ^1 : At order λ^1 , we have

$$\Phi_1(\mathbf{r}) = \frac{\bar{U}_1^{\text{cMSS}}(\mathbf{r})}{\bar{U}_0^{\text{cMSS}}(\mathbf{r})}. \quad (\text{S20})$$

The Rytov approximation of Eq. (2) is given by the first-order approximation of Eq. (S18). We set $\lambda \rightarrow 1$ and obtain $\bar{U}_{\text{Rytov}}^{\text{cMSS}}(\mathbf{r})$:

$$\begin{aligned}\bar{U}_{\text{Rytov}}^{\text{cMSS}}(\mathbf{r}) &:= \exp(\Phi_0(\mathbf{r}) + \Phi_1(\mathbf{r})) \\ &= a_0 \exp \left[\int d\mathbf{r}' V(\mathbf{r}') \frac{1}{N_{\text{in}}} \sum_j \bar{G}(\mathbf{r} - \mathbf{r}'; \mathbf{k}_{\text{in}}^j) \right].\end{aligned}\quad (\text{S21})$$

In this formulation, we applied the Rytov approximation to coherently MS-suppressed fields $\bar{U}^{\text{cMSS}}(\mathbf{r})$. As cMMS techniques suppress MS through coherent summation of fields $u(\mathbf{r}; \mathbf{k}_{\text{in}}^j)$, $\bar{U}^{\text{cMSS}}(\mathbf{r})$ is spatially smoother than $u(\mathbf{r}; \mathbf{k}_{\text{in}}^j)$. Based on this characteristic, Rytov approximation can be applied to $\bar{U}^{\text{cMSS}}(\mathbf{r})$ even if some MS exists. Therefore, the validity of the Rytov approximation expands from weak-scattering samples to MS samples owing to this formulation.

3. Formulation of iMSS-Rytov

We formulate iMSS-Rytov such that the theory of ODT is compatible with the iMSS techniques by using QPGI. QPGI is given by the phase of $\bar{W}^{\text{iMSS}}(\mathbf{r})$ in Eq. (4). We expand $\bar{W}^{\text{iMSS}}(\mathbf{r})$ as a power series in λ :

$$\begin{aligned}\bar{W}^{\text{iMSS}}(\mathbf{r}) &= \bar{W}_0^{\text{iMSS}}(\mathbf{r}) + \lambda \bar{W}_1^{\text{iMSS}}(\mathbf{r}) + \lambda^2 \bar{W}_2^{\text{iMSS}}(\mathbf{r}) + \dots \\ &= \sum_l \lambda^l \bar{W}_l^{\text{iMSS}}(\mathbf{r}).\end{aligned}\quad (\text{S22})$$

Substituting Eq. (S10) and (S22) in Eq. (4), we obtain

$$\sum_l \lambda^l \bar{W}_l^{\text{iMSS}}(\mathbf{r}) = \frac{1}{N_{\text{in}}} \sum_j \sum_l \lambda^l \bar{u}_l(\mathbf{r}; \mathbf{k}_{\text{in}}^j) \sum_m \lambda^m \bar{u}_m^*(\mathbf{r} + \delta\mathbf{r}; \mathbf{k}_{\text{in}}^j). \quad (\text{S23})$$

We can now solve Eq. (S23) by comparing coefficients of each power of λ .

Order λ^0 : At order λ^0 , we have

$$\bar{W}_0^{\text{iMSS}}(\mathbf{r}) = \frac{1}{N_{\text{in}}} \sum_j \bar{u}_0(\mathbf{r}; \mathbf{k}_{\text{in}}^j) \bar{u}_0^*(\mathbf{r} + \delta\mathbf{r}; \mathbf{k}_{\text{in}}^j) = a_0^2. \quad (\text{S24})$$

Order λ^1 : At order λ^1 , we have

$$\begin{aligned}\bar{W}_1^{\text{iMSS}}(\mathbf{r}) &= \frac{1}{N_{\text{in}}} \sum_j \bar{u}_1(\mathbf{r}; \mathbf{k}_{\text{in}}^j) \bar{u}_0^*(\mathbf{r} + \delta\mathbf{r}; \mathbf{k}_{\text{in}}^j) + \bar{u}_0(\mathbf{r}; \mathbf{k}_{\text{in}}^j) \bar{u}_1^*(\mathbf{r} + \delta\mathbf{r}; \mathbf{k}_{\text{in}}^j) \\ &= \int d\mathbf{r}' \frac{a_0^2}{N_{\text{in}}} \sum_j [\bar{G}(\mathbf{r} - \mathbf{r}'; \mathbf{k}_{\text{in}}^j) + \bar{G}^*(\mathbf{r} + \delta\mathbf{r} - \mathbf{r}'; \mathbf{k}_{\text{in}}^j)] V(\mathbf{r}').\end{aligned}\quad (\text{S25})$$

The Born approximation of Eq. (4) is given by the first-order approximation of Eq. (S22)(S23).

We set $\lambda \rightarrow 1$ and obtain $\bar{W}_{\text{Born}}^{\text{iMSS}}(\mathbf{r})$:

$$\begin{aligned}\bar{W}_{\text{Born}}^{\text{iMSS}}(\mathbf{r}) &:= \bar{W}_0^{\text{iMSS}}(\mathbf{r}) + \bar{W}_1^{\text{iMSS}}(\mathbf{r}) \\ &= a_0^2 + \int d\mathbf{r}' \frac{a_0^2}{N_{\text{in}}} \sum_j [\bar{G}(\mathbf{r} - \mathbf{r}'; \mathbf{k}_{\text{in}}^j) + \bar{G}^*(\mathbf{r} + \delta\mathbf{r} - \mathbf{r}'; \mathbf{k}_{\text{in}}^j)] V(\mathbf{r}').\end{aligned}\quad (\text{S26})$$

Next, we derive the Rytov approximation of Eq. (4). We expand $\bar{W}^{\text{iMSS}}(\mathbf{r})$ as a power series in λ , as follows:

$$\begin{aligned}\bar{W}^{\text{iMSS}}(\mathbf{r}) &= \exp(\psi_0(\mathbf{r}) + \lambda\psi_1(\mathbf{r}) + \lambda^2\psi_2(\mathbf{r}) + \dots) \\ &= \exp\left(\sum_l \lambda^l \psi_l(\mathbf{r})\right).\end{aligned}\quad (\text{S27})$$

We then equate Eq. (S22) and (S27) and solve it by comparing coefficients of each power of λ .

Order λ^0 : At order λ^0 , we have

$$\psi_0(\mathbf{r}) = \ln(\bar{W}_0^{\text{iMSS}}(\mathbf{r})). \quad (\text{S28})$$

Order λ^1 : At order λ^1 , we have

$$\psi_1(\mathbf{r}) = \frac{\bar{W}_1^{\text{iMSS}}(\mathbf{r})}{\bar{W}_0^{\text{iMSS}}(\mathbf{r})}. \quad (\text{S29})$$

The Rytov approximation of Eq. (4) is given by the first-order approximation of Eq. (S27). We set $\lambda \rightarrow 1$ and obtain $\bar{W}_{\text{Rytov}}^{\text{iMSS}}(\mathbf{r})$:

$$\begin{aligned}\bar{W}_{\text{Rytov}}^{\text{iMSS}}(\mathbf{r}) &:= \exp(\psi_0(\mathbf{r}) + \psi_1(\mathbf{r})) \\ &= a_0^2 \exp\left\{\int d\mathbf{r}' \frac{1}{N_{\text{in}}} \sum_j [\bar{G}(\mathbf{r} - \mathbf{r}'; \mathbf{k}_{\text{in}}^j) + \bar{G}^*(\mathbf{r} + \delta\mathbf{r} - \mathbf{r}'; \mathbf{k}_{\text{in}}^j)] V(\mathbf{r}')\right\}.\end{aligned}\quad (\text{S30})$$

4. Formulation of pMSS-Rytov

Here, we formulate pMSS-Rytov, which balances cMSS-Rytov and iMSS-Rytov. We show that the relationship between $\bar{W}^{\text{pMSS}}(\mathbf{r})$ and $V(\mathbf{r})$ is the same as that between $\bar{W}^{\text{iMSS}}(\mathbf{r})$ and $V(\mathbf{r})$. From Eq. (3), the Rytov approximation of $\bar{W}^{\text{cMSS}}(\mathbf{r})$ is

$$\begin{aligned}\bar{W}_{\text{Rytov}}^{\text{cMSS}}(\mathbf{r}) &:= \bar{U}_{\text{Rytov}}^{\text{cMSS}}(\mathbf{r}) \bar{U}_{\text{Rytov}}^{\text{cMSS}*}(\mathbf{r} + \delta\mathbf{r}) \\ &= a_0^2 \exp\left\{\int d\mathbf{r}' \frac{1}{N_{\text{in}}} \sum_j [\bar{G}(\mathbf{r} - \mathbf{r}'; \mathbf{k}_{\text{in}}^j) + \bar{G}^*(\mathbf{r} + \delta\mathbf{r} - \mathbf{r}'; \mathbf{k}_{\text{in}}^j)] V(\mathbf{r}')\right\}.\end{aligned}\quad (\text{S31})$$

This relationship between $\bar{W}^{\text{cMSS}}(\mathbf{r})$ and $V(\mathbf{r})$ is the same as that between $\bar{W}^{\text{iMSS}}(\mathbf{r})$ and $V(\mathbf{r})$. $\bar{W}^{\text{pMSS}}(\mathbf{r})$ lies in between $\bar{W}^{\text{cMSS}}(\mathbf{r})$ and $\bar{W}^{\text{iMSS}}(\mathbf{r})$, such that $\bar{W}^{\text{pMSS}}(\mathbf{r})$ also has the same relationship with $V(\mathbf{r})$:

$$\begin{aligned}\bar{W}^{\text{pMSS}}(\mathbf{r}) &\equiv \bar{W}_{\text{Rytov}}^{\text{pMSS}}(\mathbf{r}) \\ &= a_0^2 \exp\left\{\int d\mathbf{r}' \frac{1}{N_{\text{in}}} \sum_j [\bar{G}(\mathbf{r} - \mathbf{r}'; \mathbf{k}_{\text{in}}^j) + \bar{G}^*(\mathbf{r} + \delta\mathbf{r} - \mathbf{r}'; \mathbf{k}_{\text{in}}^j)] V(\mathbf{r}')\right\}.\end{aligned}\quad (\text{S32})$$

5. Modification to Green's function

5.1 Source-free Green's function

The Green's function must be modified because a digitally propagated field is different from the solution of the LS equation. The solution of the LS equation, $u(\mathbf{r}; \mathbf{k}_{\text{in}}^j)$, has some sources in the field: $(\nabla^2 + k_0^2)u(\mathbf{r}; \mathbf{k}_{\text{in}}^j) = -V(\mathbf{r})u(\mathbf{r}; \mathbf{k}_{\text{in}}^j)$. However, we use backpropagated fields from a detector to reconstruct the RI map, and the backpropagated field is source-free. Therefore, we

need to determine the modified Green's function, which gives the relationship between the backpropagated field and the scattering potential.

We define the field as $u^B(\mathbf{r}; \mathbf{k}_{\text{in}}^j)$, which is the backpropagated field of all the outgoing components of $u(\mathbf{r}; \mathbf{k}_{\text{in}}^j)$. Note that $u^B(\mathbf{r}; \mathbf{k}_{\text{in}}^j)$ must be a source-free field: $(\nabla^2 + k_b^2)u^B(\mathbf{r}; \mathbf{k}_{\text{in}}^j) = 0$. To derive the modified LS equation for $u^B(\mathbf{r}; \mathbf{k}_{\text{in}}^j)$, we consider the time-reversed situation in Eq. (1) (Figs. S1(a), (b)). In this time-reversed situation, the resulting field has the same spatial distribution as $u(\mathbf{r}; \mathbf{k}_{\text{in}}^j)$ but the opposite time-development direction because of the time symmetry of the wave equation. In other words, when we set the incident wave as $u^{B*}(\mathbf{r}; \mathbf{k}_{\text{in}}^j)$, the total field resulting from scattering potential $V^*(\mathbf{r})$ is equal to $u^*(\mathbf{r}; \mathbf{k}_{\text{in}}^j)$:

$$u^*(\mathbf{r}; \mathbf{k}_{\text{in}}^j) = u^{B*}(\mathbf{r}; \mathbf{k}_{\text{in}}^j) + \int G(\mathbf{r} - \mathbf{r}') V^*(\mathbf{r}') u^*(\mathbf{r}'; \mathbf{k}_{\text{in}}^j) d\mathbf{r}'. \quad (\text{S33})$$

The complex conjugate operation corresponds to a time-reversal operation. Taking the complex conjugate of this equation and equating it with Eq. (1), we obtain

$$u^B(\mathbf{r}; \mathbf{k}_{\text{in}}^j) = u_{\text{in}}(\mathbf{r}; \mathbf{k}_{\text{in}}^j) + \int [G(\mathbf{r} - \mathbf{r}') - G^*(\mathbf{r} - \mathbf{r}')] V(\mathbf{r}') u(\mathbf{r}'; \mathbf{k}_{\text{in}}^j) d\mathbf{r}', \quad (\text{S34})$$

where we assume that $V(\mathbf{r})$ is a real value. This assumption generally holds when the sample is a biological specimen. Here, $(\nabla^2 + k_b^2)u^B(\mathbf{r}; \mathbf{k}_{\text{in}}^j) = 0$ holds true because $(\nabla^2 + k_b^2)u_{\text{in}} = 0$, $(\nabla^2 + k_b^2)[G(\mathbf{r} - \mathbf{r}') - G^*(\mathbf{r} - \mathbf{r}')] = 0$, which means that $u^B(\mathbf{r}; \mathbf{k}_{\text{in}}^j)$ is a source-free field. We show examples of $u(\mathbf{r}; \mathbf{k}_{\text{in}}^j)$ and $u^B(\mathbf{r}; \mathbf{k}_{\text{in}}^j)$ in Figs. S1(d), (e).

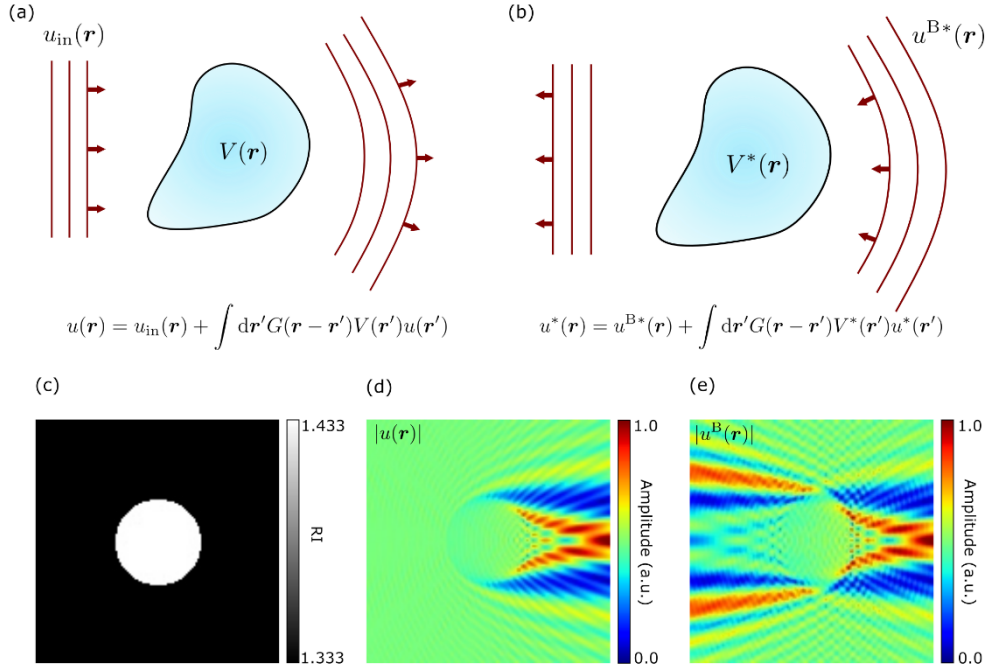


Fig. S1. Scheme of modified Green's function of our methods. (a) Time-forward scattering situation. (b) Time-reversed situation of (a). The incident field is u^B , and the resulting field is u^* , such that the spatial distribution of the resulting field is the same as in (a), except for the complex conjugate operation. (c) RI map used in (d) and (e). (d) amplitude

distribution of u determined from the RI map given in (c). (e) amplitude distribution of u^B determined from the RI map given in (c).

5.2 Limited aperture of objective lens

We must consider the limited aperture of an objective lens. The 3D pupil function of the objective lens, whose numerical aperture is NA , is given as follows:

$$P(\mathbf{k}) = \text{circ}\left(\frac{k_x^2 + k_y^2}{(k_0 NA)^2}\right) H(k_z), \quad (\text{S35})$$

where $\text{circ}(x) = 1$ if $x \leq 1$ and 0 otherwise, and $H(x) = 1$ if $x \geq 0$ and 0 otherwise. From Eqs. (S34) and (S35), we define the modified Green's function G_m :

$$G_m(\mathbf{r}) := [\mathcal{F}^{-1}(P) * (G - G^*)](\mathbf{r}), \quad (\text{S36})$$

where \mathcal{F}^{-1} is the inverse 3D Fourier transform operator.

5.3 Modification of Green's functions in cMSS-Rytov, iMSS-Rytov, and pMSS-Rytov

We modify Eq. (S21), (S30), and (S32) using Eq. (S36):

$$\bar{U}_{\text{Rytov}}^{\text{cMSS}}(\mathbf{r}; \mathbf{k}_{\text{in}}^j) = a_0 \exp \left[\int d\mathbf{r}' V(\mathbf{r}') \frac{1}{N_{\text{in}}} \sum_j \bar{G}_m(\mathbf{r} - \mathbf{r}'; \mathbf{k}_{\text{in}}^j) \right], \quad (\text{S37})$$

$$\begin{aligned} \bar{W}_{\text{Rytov}}^{\text{iMSS}}(\mathbf{r}) = \\ a_0^2 \exp \left\{ \int d\mathbf{r}' \frac{1}{N_{\text{in}}} \sum_j [\bar{G}_m(\mathbf{r} - \mathbf{r}'; \mathbf{k}_{\text{in}}^j) + \bar{G}_m^*(\mathbf{r} + \delta\mathbf{r} - \mathbf{r}'; \mathbf{k}_{\text{in}}^j)] V(\mathbf{r}') \right\}, \end{aligned} \quad (\text{S38})$$

$$\begin{aligned} \bar{W}_{\text{Rytov}}^{\text{pMSS}}(\mathbf{r}) = \\ a_0^2 \exp \left\{ \int d\mathbf{r}' \frac{1}{N_{\text{in}}} \sum_j [\bar{G}_m(\mathbf{r} - \mathbf{r}'; \mathbf{k}_{\text{in}}^j) + \bar{G}_m^*(\mathbf{r} + \delta\mathbf{r} - \mathbf{r}'; \mathbf{k}_{\text{in}}^j)] V(\mathbf{r}') \right\}. \end{aligned} \quad (\text{S39})$$

Here, $\bar{G}_m(\mathbf{r} - \mathbf{r}'; \mathbf{k}_{\text{in}}^j) := G_m(\mathbf{r} - \mathbf{r}') \exp[-i\mathbf{k}_{\text{in}}^j \cdot (\mathbf{r} - \mathbf{r}')]$. We also define

$$\mathcal{G} := \frac{1}{N_{\text{in}}} \sum_j \bar{G}_m(\mathbf{r} - \mathbf{r}'; \mathbf{k}_{\text{in}}^j), \quad (\text{S40})$$

$$\mathcal{G}^d := \frac{1}{N_{\text{in}}} \sum_j [\bar{G}_m(\mathbf{r} - \mathbf{r}'; \mathbf{k}_{\text{in}}^j) + \bar{G}_m^*(\mathbf{r} + \delta\mathbf{r} - \mathbf{r}'; \mathbf{k}_{\text{in}}^j)]. \quad (\text{S41})$$

6. Deconvolution algorithm

6.1 cMSS-Rytov

cMSS-Rytov reconstructs the RI map from confocal QPI images by deconvolution, whose kernel is given by the summation of modified Green's functions (Supplementary Section 5). Here, let G , v , and ϕ be the kernel given by Eq. (S41), vector representation of the scattering potential, and vector representation of the 3D confocal QPI image, respectively. We also introduce a cropping operator [2] D to avoid aliasing, as the kernel is heavy-tailed. The estimation of v from ϕ is given by the following optimization problem:

$$\min_{v \geq 0} \|\phi - \text{DG}v\|_2^2. \quad (\text{S42})$$

This problem was solved using the alternating direction method of multipliers (ADMM) [3]. The program was stopped after 50 iterations.

6.2 iMSS-Rytov and pMSS-Rytov

iMSS-Rytov and pMSS-Rytov reconstruct the RI distribution from QPGI images by deconvolution. Here, let G_x^d, G_y^d, ψ_x , and ψ_y be the discretized derivative of the 3D Green's function with respect to x , the discretized derivative of the 3D Green's function with respect to y (Eq. (S41)), vector representation of QPGI differentiated with respect to x , and vector representation of QPGI differentiated with respect to y , respectively. Unlike QPI, QPGI does not have a constant component owing to its differentiation operation; hence, the estimated v is also uncertain about its constant value. To address this problem, the estimation of v was performed using the following optimization problem:

$$\min_{v \geq 0} \frac{1}{2} \|\psi_x - \text{DG}_x^d v\|_2^2 + \frac{1}{2} \|\psi_y - \text{DG}_y^d v\|_2^2 + \frac{\xi}{2} \|v\|_1. \quad (\text{S43})$$

The L1-norm term was introduced to limit the range of v to near-zero values. This term and the nonnegativity constraint help the solution converge to the accurate solution. If ξ is too large, the estimated RI distribution can be different from the exact values. We chose $\xi = 0.1$ for simulation and 0.2 for experiments. The shear amount of QPGI is set as $\lambda_0/7.5$ in simulations and 420 nm in experiments, respectively. The optimization problem was solved using ADMM, and the program was stopped after 50 iterations.

7. Pseudo code for the reconstruction of phase maps through the cMSS, iMSS and pMSS techniques

Tables S1, S2 and S3 present the pseudo-code for the reconstructions of phase maps $\angle \bar{U}^{\text{cMSS}}(\mathbf{r})$, $\angle \bar{W}^{\text{iMSS}}(\mathbf{r})$ and $\angle \bar{W}^{\text{pMSS}}(\mathbf{r})$ from measured complex fields, respectively.

Table S1. Pseudo code for $\angle \bar{U}^{\text{cMSS}}(\mathbf{r})$ calculation

Input	
$\{w(\boldsymbol{\rho})\}_{j=1}^{N_{\text{in}}}$:	Measured complex fields at initial position $z=0$, where $\boldsymbol{\rho} = (x,y)$ and N_{in} is the total number of incident angles
$\{\mathbf{k}_{\text{in}}^j\}_{j=1}^{N_{\text{in}}}$:	3D incident wavevectors of $\{w(\boldsymbol{\rho})\}_{j=1}^{N_{\text{in}}}$
Δz :	step size in z direction
N_{layer} :	the number of layers in z direction
k_b :	the wavenumber in the medium
Initialization	
$\{\bar{U}^{\text{cMSS}}(\boldsymbol{\rho}, n\Delta z)\}_{n=1}^{N_{\text{layer}}}$	$= 0$
1. for $n \leftarrow 1$ to N_{layer} do	
2. for $j \leftarrow 1$ to N_{in} do	
3. $\mathbf{r} \leftarrow (\boldsymbol{\rho}, n\Delta z)$	
4. $u_{\text{prop}}(\boldsymbol{\rho}) \leftarrow \mathcal{F}^{-1}\{\mathcal{F}\{w(\boldsymbol{\rho})\} \exp(i\sqrt{k_b^2 - \ \mathbf{k}_T\ _2^2} n\Delta z)\}$	(Digital propagation, where \mathbf{k}_T is the 2D wavevector coordinates corresponding to $\boldsymbol{\rho}$ and \mathcal{F} is Fourier transform operator)
5. $\bar{u}_{\text{prop}}(\boldsymbol{\rho}) \leftarrow u_{\text{prop}}(\boldsymbol{\rho}) \exp(i\mathbf{k}_{\text{in}}^j \cdot \mathbf{r})$	
6. $\bar{U}^{\text{cMSS}}(\boldsymbol{\rho}, n\Delta z) \leftarrow \bar{U}^{\text{cMSS}}(\boldsymbol{\rho}, n\Delta z) + \bar{u}_{\text{prop}}(\boldsymbol{\rho})$	
7. $\bar{U}^{\text{cMSS}}(\boldsymbol{\rho}, n\Delta z) \leftarrow \bar{U}^{\text{cMSS}}(\boldsymbol{\rho}, n\Delta z)/N_{\text{in}}$	

Return

$$\{\angle \bar{U}^{\text{cMSS}}(\boldsymbol{\rho}, n\Delta z)\}_{n=1}^{N_{\text{layer}}}$$

Table S2. Pseudo code for $\angle \bar{W}^{\text{IMSS}}(r)$ calculation

Input

$\{\mathbf{w}(\boldsymbol{\rho})\}_{j=1}^{N_{\text{in}}}$: Measured complex fields at initial position $z=0$, where $\boldsymbol{\rho} = (x,y)$ and N_{in} is the total number of incident angles

$$\{\mathbf{k}_{\text{in}}^j\}_{j=1}^{N_{\text{in}}} : N_{\text{in}} \text{ 3D incident wavevectors of } \{u^j(\boldsymbol{\rho})\}_{j=1}^{N_{\text{in}}}$$
 $\delta \boldsymbol{\rho}$: 2D shear vector Δz : step size in z direction

N_{layer} : the number of layers in z direction

k_b : the wavenumber in the medium

Initialization

$$\{\overline{W}^{\text{iMSS}}(\boldsymbol{\rho}, n\Delta z)\}_{n=1}^{N_{\text{layer}}} = 0$$
1. **for** $n \leftarrow 1$ **to** N_{layer} **do**2. **for** $j \leftarrow 1$ **to** N_{in} **do**3. $\mathbf{r} \leftarrow (\boldsymbol{\rho}, n\Delta z)$
$$4. \quad u_{\text{prop}}(\boldsymbol{\rho}) \leftarrow \mathcal{F}^{-1} \{ \mathcal{F} \{ u^j(\boldsymbol{\rho}) \} \exp(i\sqrt{k_b^2 - \|\mathbf{k}_T\|_2^2} n\Delta z) \}$$

(Digital propagation, where \mathbf{k}_T is the 2D wavevector coordinates corresponding to $\boldsymbol{\rho}$ and \mathcal{F} is Fourier transform operator)

5. $\bar{u}_{\text{prop}}(\boldsymbol{\rho}) \leftarrow u_{\text{prop}}(\boldsymbol{\rho}) \exp(i\mathbf{k}_{\text{in}}^j \cdot \mathbf{r})$

$$6. \quad \bar{W}^{\text{iMSS}}(\boldsymbol{\rho}, n\Delta z) \leftarrow \bar{W}^{\text{iMSS}}(\boldsymbol{\rho}, n\Delta z) + \bar{u}_{\text{prop}}(\boldsymbol{\rho}) \bar{u}_{\text{prop}}^*(\boldsymbol{\rho} + \delta\boldsymbol{\rho})$$
$$7. \quad \bar{W}^{\text{iMSS}}(\rho, n\Delta z) \leftarrow \bar{W}^{\text{iMSS}}(\rho, n\Delta z)/N_{\text{in}}$$

8. $\angle \bar{W}^{\text{iMSS}}(\rho, n\Delta z) \leftarrow \text{Angle}(\bar{W}^{\text{iMSS}}(\rho, n\Delta z))$

Return

$$\{\angle \overline{W}^{\text{iMSS}}(\boldsymbol{\rho}, n\Delta z)\}_{n=1}^{N_{\text{layer}}}$$

Table S3. Pseudo code for $\angle \bar{W}^{\text{pMSS}}(r)$ calculation

Input

$\{w^j(\boldsymbol{\rho})\}_{j=1}^{N_{\text{in}}}$: Measured complex fields at initial position $z=0$, where $\boldsymbol{\rho} = (x, y)$ and N_{in} is the total number of incident angles

$$\{\mathbf{k}_{\text{in}}^j\}_{j=1}^{N_{\text{in}}} : \text{3D incident wavevectors of } \{w^j(\boldsymbol{\rho})\}_{j=1}^{N_{\text{in}}}$$
 $\delta \boldsymbol{\rho}$: 2D shear vector γ : tuning parameter Δz : step size in z direction

N_{layer} : the number of layers in z direction

k_b : the wavenumber in the medium

Initialization

$$\{\overline{U}^{\text{cMSS}}(\boldsymbol{\rho}, n\Delta z)\}_{n=1}^{N_{\text{layer}}} = 0$$
$$\{\overline{W}^{\text{iMSS}}(\boldsymbol{\rho}, n\Delta z)\}_{n=1}^{N_{\text{layer}}} = 0$$
$$\{\overline{W}^M(\rho, n\Delta z)\}_{n=1}^{N_{\text{layer}}} = 0$$
1. **for** $n \leftarrow 1$ **to** N_{layer} **do**2. **for** $j \leftarrow 1$ **to** N_{in} **do**3. $\mathbf{r} \leftarrow (\boldsymbol{\rho}, n\Delta z)$

```

4.  $u_{\text{prop}}^j(\boldsymbol{\rho}) \leftarrow \mathcal{F}^{-1}\{\mathcal{F}\{u^j(\boldsymbol{\rho})\} \exp(i\sqrt{k_b^2 - \|\mathbf{k}_T\|_2^2} n\Delta z)\}$ 
   (Digital propagation, where  $\mathbf{k}_T$  is the 2D wavevector coordinates corresponding to  $\boldsymbol{\rho}$ 
   and  $\mathcal{F}$  is Fourier transform operator)
5.  $\bar{u}_{\text{prop}}^j(\boldsymbol{\rho}) \leftarrow u_{\text{prop}}^j(\boldsymbol{\rho}) \exp(i\mathbf{k}_{\text{in}}^j \cdot \mathbf{r})$ 
6.  $\bar{U}^{\text{cMSS}}(\boldsymbol{\rho}, n\Delta z) \leftarrow \bar{U}^{\text{cMSS}}(\boldsymbol{\rho}, n\Delta z) + \bar{u}_{\text{prop}}^j(\boldsymbol{\rho})$ 
7.  $\bar{W}^{\text{iMSS}}(\boldsymbol{\rho}, n\Delta z) \leftarrow \bar{W}^{\text{iMSS}}(\boldsymbol{\rho}, n\Delta z) + \bar{u}_{\text{prop}}^j(\boldsymbol{\rho}) \bar{u}_{\text{prop}}^{j*}(\boldsymbol{\rho} + \delta\boldsymbol{\rho})$ 
8.  $\bar{W}^{\text{iMSS}}(\boldsymbol{\rho}, n\Delta z) \leftarrow \bar{W}^{\text{iMSS}}(\boldsymbol{\rho}, n\Delta z) / N_{\text{in}}$ 
9.  $\bar{U}^{\text{cMSS}}(\boldsymbol{\rho}, n\Delta z) \leftarrow \bar{U}^{\text{cMSS}}(\boldsymbol{\rho}, n\Delta z) / N_{\text{in}}$ 
10. for  $j \leftarrow 1$  to  $N_{\text{in}}$  do
11.  $\bar{u}_{\text{prop}}^M(\boldsymbol{\rho}) \leftarrow \bar{u}_{\text{prop}}^j(\boldsymbol{\rho}) - \bar{U}^{\text{cMSS}}(\boldsymbol{\rho}, n\Delta z)$ 
12.  $\bar{W}^M(\boldsymbol{\rho}, n\Delta z) \leftarrow \bar{W}^M(\boldsymbol{\rho}, n\Delta z) + \bar{u}_{\text{prop}}^M(\boldsymbol{\rho}) \bar{u}_{\text{prop}}^{M*}(\boldsymbol{\rho} + \delta\boldsymbol{\rho})$ 
13.  $\bar{W}^M(\boldsymbol{\rho}, n\Delta z) \leftarrow \bar{W}^M(\boldsymbol{\rho}, n\Delta z) / N_{\text{in}}$ 
14.  $\bar{W}^{\text{pMSS}}(\boldsymbol{\rho}, n\Delta z) \leftarrow \bar{W}^{\text{iMSS}}(\boldsymbol{\rho}, n\Delta z) - \gamma \bar{W}^M(\boldsymbol{\rho}, n\Delta z)$ 
15.  $\angle \bar{W}^{\text{pMSS}}(\boldsymbol{\rho}, n\Delta z) \leftarrow \text{Angle}(\bar{W}^{\text{pMSS}}(\boldsymbol{\rho}, n\Delta z))$ 

Return
 $\{\angle \bar{W}^{\text{pMSS}}(\boldsymbol{\rho}, n\Delta z)\}_{n=1}^{N_{\text{layer}}}$ 

```

8. Numerical simulation of cell phantom

To validate that our approach visualizes the subcellular structure of cell samples, we applied our methods to a cell phantom immersed in water (RI $n = 1.333$). The cell phantom (Fig. S2(a)) comprises the cytoplasm ($n = 1.360$), nucleus ($n = 1.350$), nucleolus ($n = 1.365$), and several small organelles ($n = 1.370$), within a volume of $128 \times 128 \times 128$ voxels with $\lambda_0/7.5$ resolution. The simulated fields with an illumination angle $\theta_x, \theta_y = 0^\circ, 43.4^\circ$ and reconstruction results of our proposed methods are shown in Figs. S2(b) and (c). All methods succeeded in visualizing subcellular structures inside the cell phantom. Therefore, our methods have the resolving power to visualize the subcellular structure.

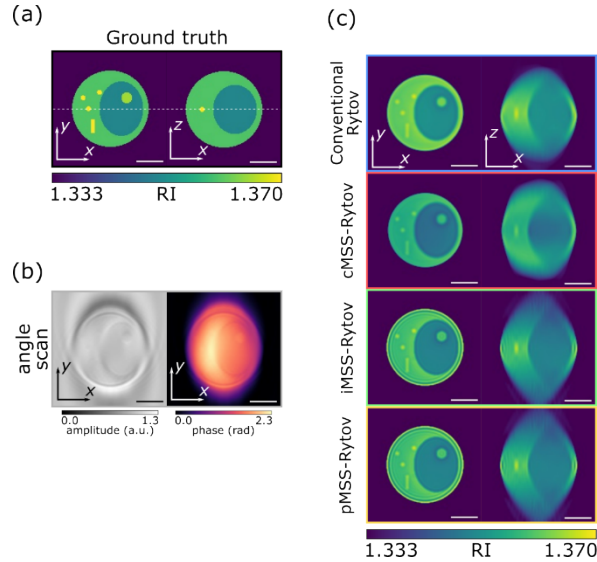


Fig. S2. Simulations using a cell phantom. (a) x-y and x-z cross-sections of the ground truth of the RI map of the cell. (b) Simulated fields with an illumination angle $\theta_x, \theta_y = 0^\circ, 43.4^\circ$. (c) x-y and x-z cross-sections of RI distributions obtained by Conventional Rytov, cMSS-Rytov, iMSS-Rytov, and pMSS-Rytov, respectively. Scale bars: $5\lambda_0$.

9. Comparison of forward models

We evaluated the forward model accuracy of each model using the model in Fig. 3. The left column of Fig.S3(a) shows true fields calculated using the SEAGLE forward model. $u(\mathbf{r}; \mathbf{k}_{\text{in}}^j)$ was calculated using the SEAGLE forward model, and $\angle \bar{U}^{\text{cMSS}}(\mathbf{r})$, $\angle \bar{W}^{\text{iMSS}}(\mathbf{r})$, and $\angle \bar{W}^{\text{pMSS}}(\mathbf{r})$ were calculated from $u(\mathbf{r}; \mathbf{k}_{\text{in}}^j)$ using Eqs. (2), (4) and (7), respectively. The right column of Fig.S3(a) shows fields calculated using each forward model. $u_{\text{Rytov}}(\mathbf{r}; \mathbf{k}_{\text{in}}^j)$, $\angle \bar{U}_{\text{Rytov}}^{\text{cMSS}}(\mathbf{r})$, $\angle \bar{W}_{\text{Rytov}}^{\text{iMSS}}(\mathbf{r})$, and $\angle \bar{W}_{\text{Rytov}}^{\text{pMSS}}(\mathbf{r})$ were calculated using Eqs. (S9), (S37),

(S38), and (S39), respectively. Fig.S3(b) shows the error of these fields. We also quantitatively evaluated the performance of each method with the normalized data fit (NDF) defined as

$$\text{NDF}(y_{\text{true}}, y_{\text{recon}}) := \frac{\|y_{\text{recon}} - y_{\text{true}}\|_2^2}{\|y_{\text{true}}\|_2^2} \quad (\text{S44})$$

where y_{true} is the true field calculated using results of SEAGLE and y_{recon} is calculated using each forward model. Hence, $(y_{\text{true}}, y_{\text{recon}}) = (u(\mathbf{r}; \mathbf{k}_{\text{in}}^j), u_{\text{Rytov}}(\mathbf{r}; \mathbf{k}_{\text{in}}^j)), (\angle \bar{U}^{\text{cMSS}}(\mathbf{r}), \angle \bar{U}_{\text{Rytov}}^{\text{cMSS}}(\mathbf{r})), (\angle \bar{W}^{\text{iMSS}}(\mathbf{r}), \angle \bar{W}_{\text{Rytov}}^{\text{iMSS}}(\mathbf{r})), (\angle \bar{W}^{\text{pMSS}}(\mathbf{r}), \angle \bar{W}_{\text{Rytov}}^{\text{pMSS}}(\mathbf{r}))$. The NDF of conventional Rytov, cMSS-Rytov, iMSS-Rytov and pMSS-Rytov was 0.152, 0.004, 0.144 and 0.086, respectively. According to the NDF, the three proposed methods have higher forward-model accuracy than conventional Rytov.

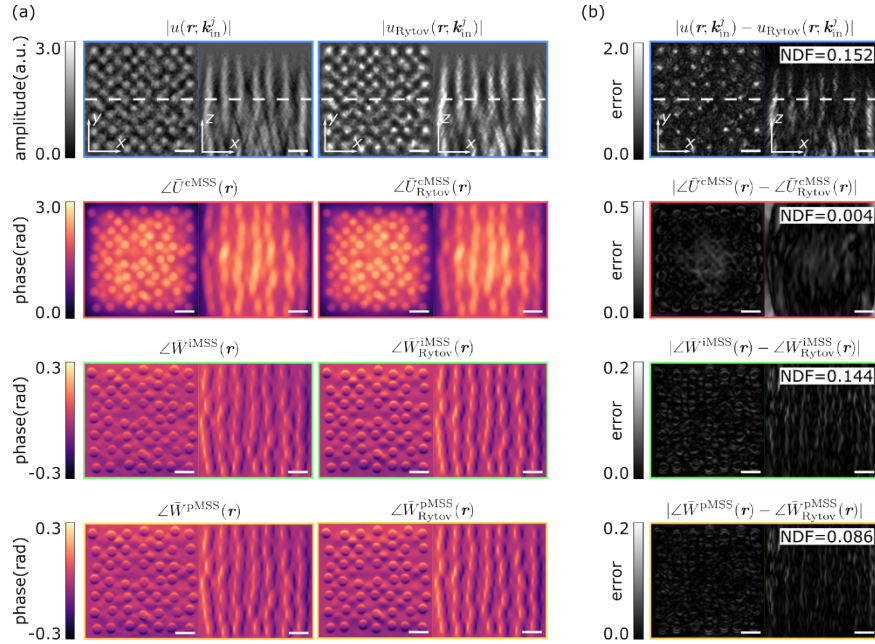


Fig. S3. The forward model accuracy of each method. (a) The left column of Fig.S3(a) shows true fields calculated using the SEAGLE forward model. The right column of Fig.S3(a) shows fields calculated using each forward model. (b) The error of fields shown in (a). The normalized data fit (NDF) of conventional Rytov, cMSS-Rytov, iMSS-Rytov and pMSS-Rytov was 0.152, 0.004, 0.144 and 0.086, respectively.

10. Experimental setup

We constructed a transmission-mode interferometric microscope with a Mach–Zehnder configuration (Fig. S4). We used a He–Ne laser (632.8 nm, 5 mW) as the light source. The light was coupled into a single-mode fiber and split into a sample beam and a reference beam using a beam splitter (BS1). The sample beam was illuminated onto the sample at various angles of incidence using a 2D scanning mirror (Optotune). We set the scanning pattern as a grid pattern, such that the numerical aperture of incidence equaled 0.9. The sample was placed between a condenser lens (OB1, Olympus, 60 \times , 1.0NA, water immersion) and an objective lens (OB2, Olympus, 60 \times , 1.0NA, water immersion). The scattered light from the sample was projected onto a CMOS camera (GO-2400M-USB, JAI) using a 4f system consisting of OB1 and a tube lens ($f = 125$ mm) after combining with the reference beam at another beam splitter (BS2). On the camera plane, the sample beam interfered with the reference beam, which was slightly tilted against the propagation direction of the sample beam to generate off-axis interferograms. To reconstruct a 3D RI tomogram, we recorded 441 holograms of the sample at a frame rate of 62 fps, which required 7 s.

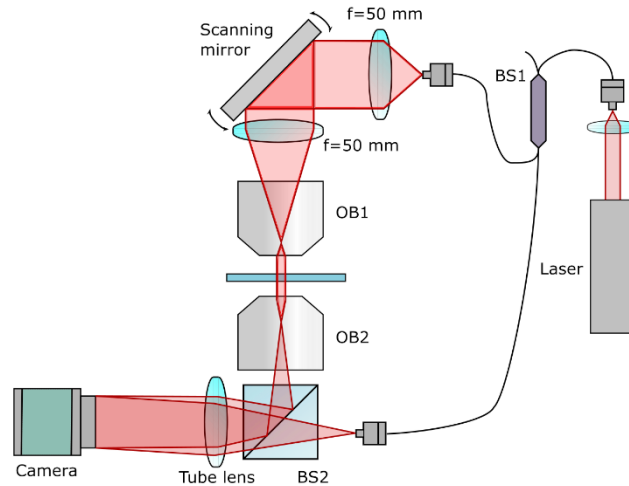


Fig. S4. Experimental setup. BS1, BS2: beam splitters. The magnification from the sample plane to the camera was 41.7 \times .

11. Preparation of cellular samples

The human breast cancer cell line, MCF-7, was obtained from the European Collection of Cell Cultures and cultured in an advanced minimum essential medium (Gibco) supplemented with 2.5% (v/v) fetal bovine serum (FBS, Gibco), 100 U/mL of penicillin, 100 μ g/mL of streptomycin, and 292 μ g/mL of L-glutamine (1 \times Penicillin-Streptomycin-Glutamine, Gibco). The human hepatoma HepG2 cell line (JCRB1054) [4] was obtained from the Japanese Collection of Research Bioresources and cultured in Dulbecco's modified Eagle's medium (DMEM, Gibco) supplemented with 10% (v/v) FBS (Gibco) and 1 \times penicillin-streptomycin-glutamine (Gibco). Multicellular spheroids were formed using a 3D cell culture container, the EZSPHERE 6-well plate (AGC Techno Glass). MCF-7 cells were seeded at 35,000 cells per well in 2 mL of the culture medium and incubated for 1 d to allow spheroid formation. HepG2 cells were seeded at 30,000 cells per well in 2 mL of the culture medium and incubated for 2 d to form spheroids. To induce lipid-droplet formation in HepG2 spheroids, the medium was replaced with phenol-red-free DMEM (Gibco) containing 1% (w/v) fatty-acid-free bovine serum albumin (BSA, FUJIFILM Wako Pure Chemical) and 0.5 mM sodium oleate (Nacalai Tesque) 1 d after seeding, and the spheroids were further cultured for 1 d. All cell samples were cultured at 37 $^{\circ}$ C in 5% CO₂ humidified atmosphere. The spheroids were washed in phosphate-

buffered saline (Gibco) or Hanks' balanced salt solution (Gibco) and collected via centrifugation at $150 \times g$ for 3 min.

12. Numerical aberration estimation

In general, the aberration of an optical system is expressed as a phase map in the pupil plane. In most cases, the phase map is expressed as the sum of orthogonal modes, such as Zernike polynomials. Our strategy to identify the system aberration is to automatically estimate the coefficients of Zernike polynomials that maximize a sharpness metric calculated from aberration corrected images. As the metric to determine the coefficients, we used QPGI image given by Eq. (4), which is given by the incoherent summation of the angle-scanned complex fields. We define the sharpness metric S using QPGI as follows:

$$S := \sum_r |\angle \bar{W}^{\text{IMSS}}(\mathbf{r})|^3. \quad (\text{S45})$$

Using this metric, we estimated 4th to 28th-order coefficients of Zernike polynomials. The order of Zernike polynomials follows Noll's sequential indices [5]. To automatically optimize the coefficients, we used the particle swarm optimization (PSO) algorithm [6]. The number of particles of PSO was set to 100, and the particle parameters were initialized with a Gaussian distribution with standard deviation $\sigma=1$. Two-hundred iterations of PSO were performed. Polystyrene beads were used as the target image for the optimization. Figures S5(a) and (b) show the estimated aberration map and coefficients of Zernike polynomials, respectively. Figure S5(c) shows the QPGI image of a polystyrene bead used as the target image before and after aberration correction, respectively. Compared to the former, the latter is sharper and has higher peak phase values. This result indicates that aberration correction was successful. Using the estimated aberration map, we also performed aberration correction to the image of an MCF-7 cell used in Fig. 5. Figs. S5(d) and (e) show the MIPs of the RI distributions before and after aberration correction. In the case without aberration correction, the RI map by conventional Rytov (the left column of Figs. S5(d)) shows a nonuniform distribution with high values in the upper-half and low values in the lower-half of z-direction. On the contrary, the RI distribution by conventional Rytov with aberration correction (the left column of Figs. S5(e)) is more uniform. In addition, in both the conventional Rytov and the proposed methods, the RI distributions after aberration correction visualize the detailed intracellular structures more successfully (Figs. S5(e)) compared to the case without aberration correction (Fig. S5(d)).

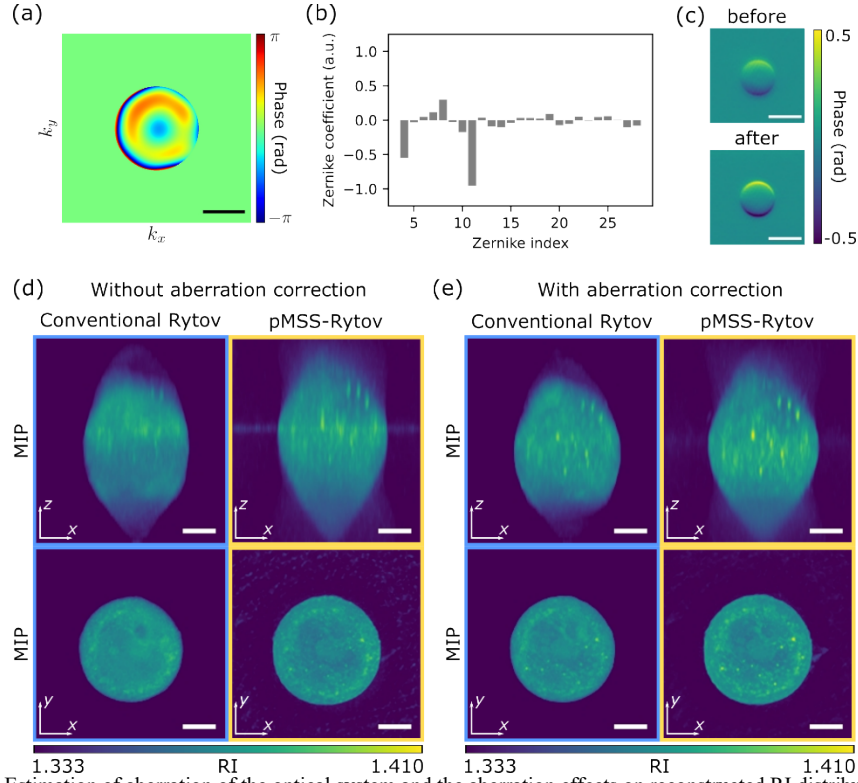


Fig. S5. Estimation of aberration of the optical system and the aberration effects on reconstructed RI distributions. (a) The estimated aberration maps. Scale bar, $k_o NA$. (b) The estimated the 4th to 28th-order coefficients of Zernike polynomials following the convention of Noll's sequential indices. (c) QPGI images of a polystyrene bead before and after aberration correction. (d-e) The RI distribution of an MCF-7 cell used in Fig. 5 with and without aberration correction, respectively.

13. Complex fields of captured data in experiments

Figure S.6 shows complex fields with incident angles $(\theta_x, \theta_y) = (0.0^\circ, 0.0^\circ), (-27.0^\circ, 7.2^\circ)$ of the samples shown in Figs. 5, 6, 7. These images are reconstructed by digital holographic technique from raw intensity images to complex fields. The phase images of multicellular spheroids contain lots of discontinuities of the phase, which leads to the loss of the image fidelity of reconstructed RI distributions.

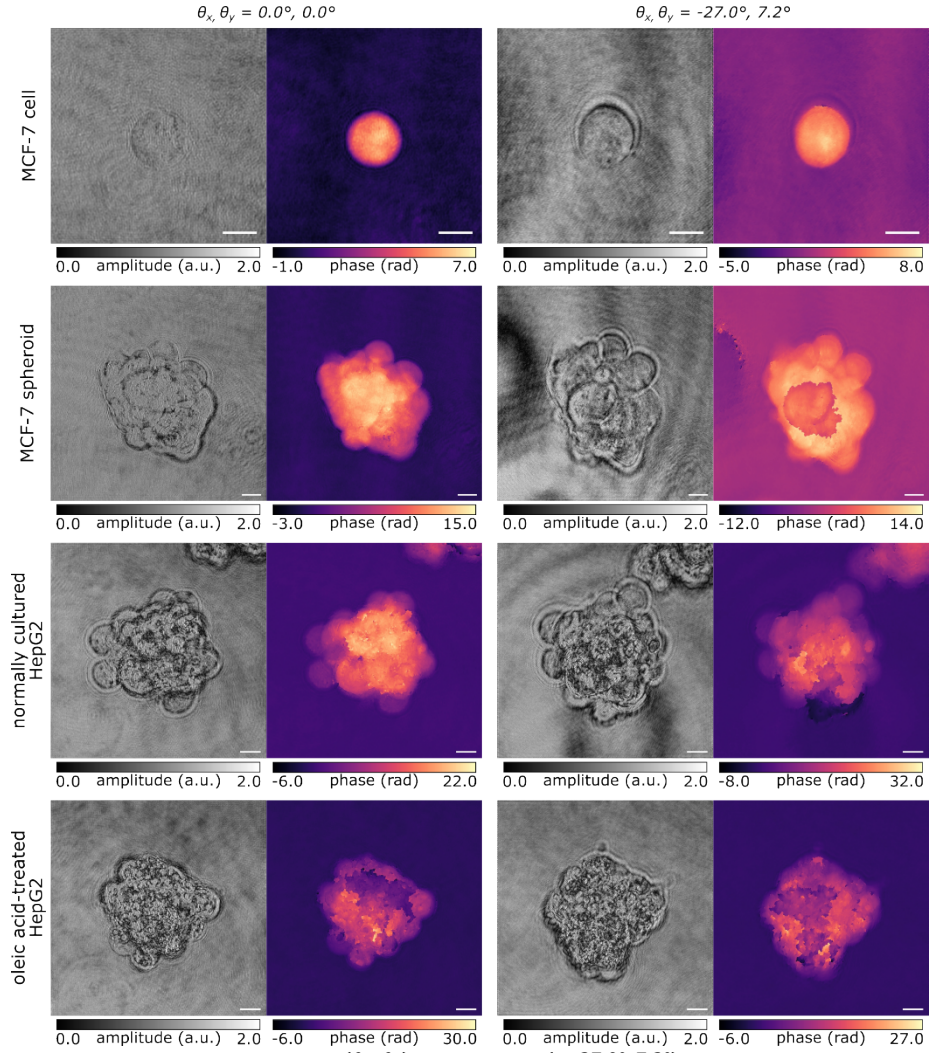


Fig. S6. Complex fields with incident angles $(\theta_x, \theta_y) = (0.0^\circ, 0.0^\circ), (-27.0^\circ, 7.2^\circ)$ of the samples in Fig. 5, 6, 7. Scale bars: 10 μm

14. Phase distributions of captured data in experiments

Figure S.7 shows phase distributions, $\angle \bar{U}^{\text{cMSS}}(\mathbf{r})$, $\angle \bar{W}^{\text{iMSS}}(\mathbf{r})$ and $\angle \bar{W}^{\text{pMSS}}(\mathbf{r})$, of the samples shown in Figs. 5, 6 and 7. These images are calculated by Eqs. (2), (4) and (7) from complex fields shown in Fig. S6. $\angle \bar{U}^{\text{cMSS}}(\mathbf{r})$ has many phase discontinuities around the edge of the samples due to SIA of spheroids. On the other hand, $\angle \bar{W}^{\text{iMSS}}(\mathbf{r})$ and $\angle \bar{W}^{\text{pMSS}}(\mathbf{r})$ do not have such phase discontinuities.

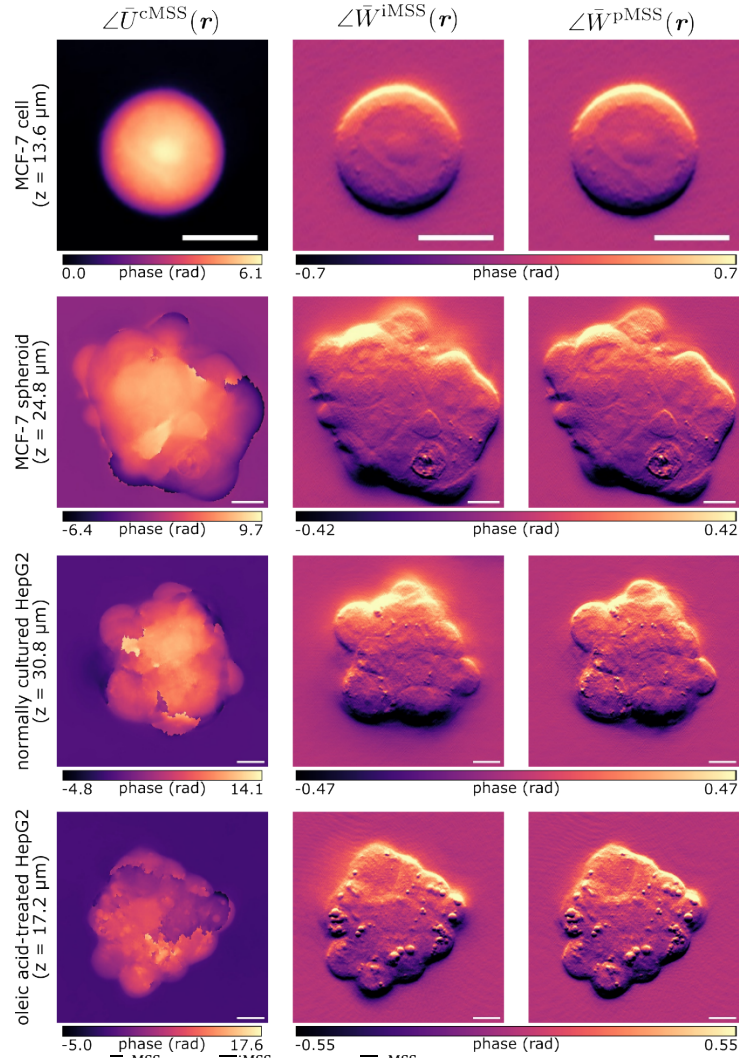


Fig. S7. Phase distributions, $\angle \bar{U}^{cMSS}(\mathbf{r})$, $\angle \bar{W}^{iMSS}(\mathbf{r})$ and $\angle \bar{W}^{pMSS}(\mathbf{r})$, of the samples shown in Figs. 5, 6, 7. Scale bars: 10 μm

15. RI distributions of HepG2 reconstructed by conventional Rytov

We present the RI maps of normally cultured and oleic-acid-treated HepG2 spheroids obtained by conventional Rytov approximation (Fig. S8). According to Fig. S8, conventional Rytov approximation failed to visualize lipid-droplet structures that can be observed by pMSS-Rytov, as shown in Fig. 7.

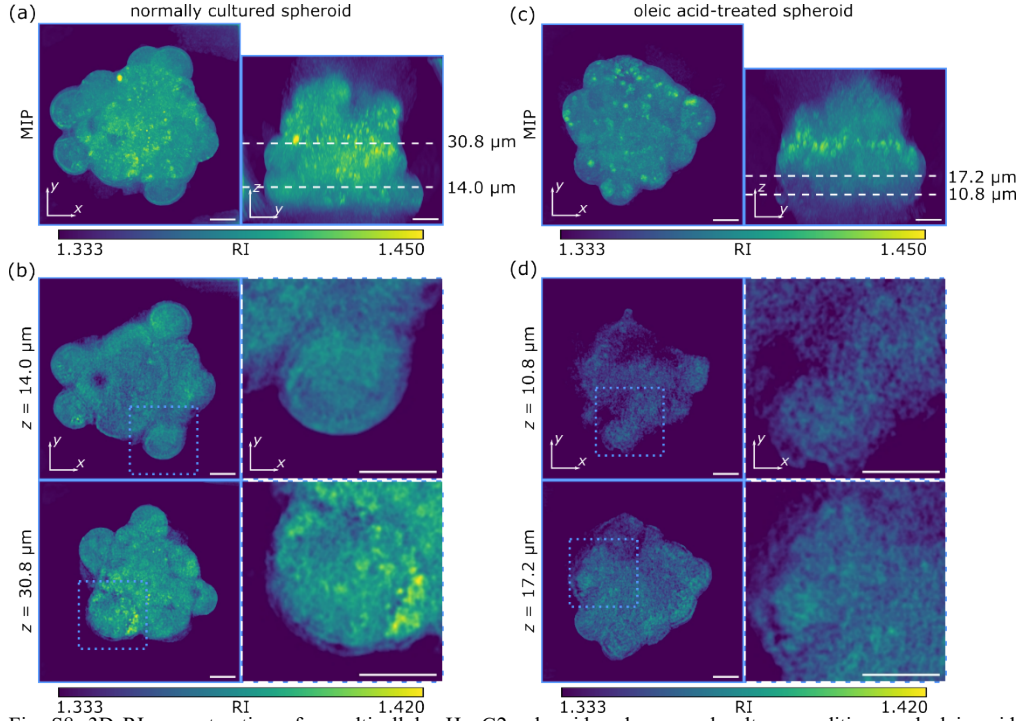


Fig. S8. 3D RI reconstruction of a multicellular HepG2 spheroid under normal culture conditions and oleic acid induction reconstructed by Conventional Rytov. (a-b) MIPs in two different planes and x-y cross section along the white dotted line in (a) of the normally cultured HepG2 spheroid. (c-d) MIPs in two different planes and x-y cross section along the white dotted line in (d) of the oleic-acid-treated HepG2 spheroid. The lipid droplets observed in Fig. 7 are hard to recognize in this figure owing to the limitation of conventional Rytov approximation. Scale bars: 10 μm

16. Computational cost of our method and BPM-based approach

First, we consider the complexity of the BPM-based approach. In the BPM case, $2N$ 2D-FFT is required for end-to-end propagation for each angle of incidence. Therefore, for the end-to-end propagation for all angles of incidence, it requires a complexity of $O(N_{\text{angle}}N^3\log N)$. The same complexity is necessary for backpropagation. The BPM-based approach repeats this computation N_{iter} times for optimization. As a result, it requires a complexity of $O(N_{\text{iter}}N_{\text{angle}}N^3\log N)$.

Next, we consider the complexity of our approach, which first calculates a multiple-scattering suppressed image from angle-scanned data. Similar to the forward process of the BPM approach, it requires a complexity of $O(N_{\text{angle}}N^3\log N)$. Subsequently, we calculate the RI distribution for the multiple-scattering suppressed image using ADMM. In our implementation of pMSS-Rytov, 7 3D-FFT are required for each iteration, requiring a complexity of $O(N_{\text{iter}}N^3\log N)$ for all iterations. As a result, the complexity of our approach is $O(N_{\text{angle}}N^3\log N) + O(N_{\text{iter}}N^3\log N)$.

Reference

1. G. Potvin, "General Rytov approximation," J. Opt. Soc. Am. A **32**, 1848–1856 (2015).
2. N. Antipa, G. Kuo, R. Heckel, B. Mildenhall, E. Bostan, R. Ng, and L. Waller, "DiffuserCam: lensless single-exposure 3D imaging," Optica **5**, 1–9 (2018).
3. S. Boyd, N. Parikh, E. Chu, B. Peleato, and J. Eckstein, "Distributed Optimization and Statistical Learning via the Alternating Direction Method of Multipliers," Found. Trends Mach. Learn. **3**, 1–122 (2011).
4. D. P. Aden, A. Fogel, S. Plotkin, I. Damjanov, and B. B. Knowles, "Controlled synthesis of HBsAg in a differentiated human liver carcinoma-derived cell line," Nature **282**, 615–616 (1979).
5. R. J. Noll, "Zernike polynomials and atmospheric turbulence*," J. Opt. Soc. Am. **66**, 207–211 (1976).

6. J. Kennedy and R. Eberhart, "Particle swarm optimization," in *Proceedings of ICNN'95 - International Conference on Neural Networks* (1995), Vol. 4, pp. 1942–1948 vol.4.